Phonon and magnon scattering of antiferromagnetic $Bi_2Fe_4O_9$

M. N. Iliev, A. P. Litvinchuk, and V. G. Hadjiev
Texas Center for Superconductivity, University of Houston, Texas 77204-5002, USA

M. M. Gospodinov
Institute of Solid State Physics, Bulgarian Academy of Sciences, 1184 Sofia, Bulgaria

V. Skumryev
Institució Catalana de Recerca i Estudis Avançats (ICREA) and Departament de Física, Universitat Autònoma de Barcelona, 08193 Bellaterra, Spain

E. Ressouche
Département de Recherche Fondamentale sur la Matière Condensée, SPSMS, CEA-Grenoble, Grenoble 38054, France
(Received 24 September 2009; revised manuscript received 25 November 2009; published 5 January 2010)

The phonon structure of antiferromagnetic $Bi_2Fe_4O_9$ (space group *Pbnm* No. 55, $T_N \approx 240$ K) was studied theoretically by calculations of lattice dynamics and experimentally between 10 and 300 K by polarized Raman spectroscopy. Most of the $12A_g+12B_{1g}+9B_{2g}+9B_{3g}$ Raman modes were unambiguously identified. Strong second-order scattering was observed for *ab*-plane-confined incident and scattered light polarizations. In addition to the phonon-scattering, broad Raman bands with typical characteristics of magnon scattering appear below T_N. The magnon bands are analyzed on the basis of magnetic structure of $Bi_2Fe_4O_9$ and attributed to two-magnon excitations.

DOI: 10.1103/PhysRevB.81.024302 PACS number(s): 78.30.−j, 77.84.Bw, 63.20.−e, 75.50.Ee

I. INTRODUCTION

The crystallographic structure of $Bi_2Fe_4O_9$, shown in Fig. 1, belongs to the orthorhombic space group *Pbam*, No. 55, with two formula units per unit cell.[1,2] It can be described by columns of edge-sharing $Fe(2)O_6$ octahedra parallel to the *c* axis, linked by corner-sharing $Fe(1)O_4$ tetrahedra and Bi atoms. With lowering temperature below $T_N \approx 240-265$ K the compound undergoes a transition to an antiferromagnetic state. The larger unit cell of the magnetic structure is monoclinic P_c2/m with unit-cell vectors parameters $\mathbf{a_m}=2\mathbf{a_o}$, $\mathbf{b_m}=2\mathbf{c_o}$, and $\mathbf{c_m}=-\mathbf{a_o}-\mathbf{b_o}$, and all magnetic moments are perpendicular to the $\mathbf{c_o}$ ($\mathbf{b_m}$) axis.[2,3]

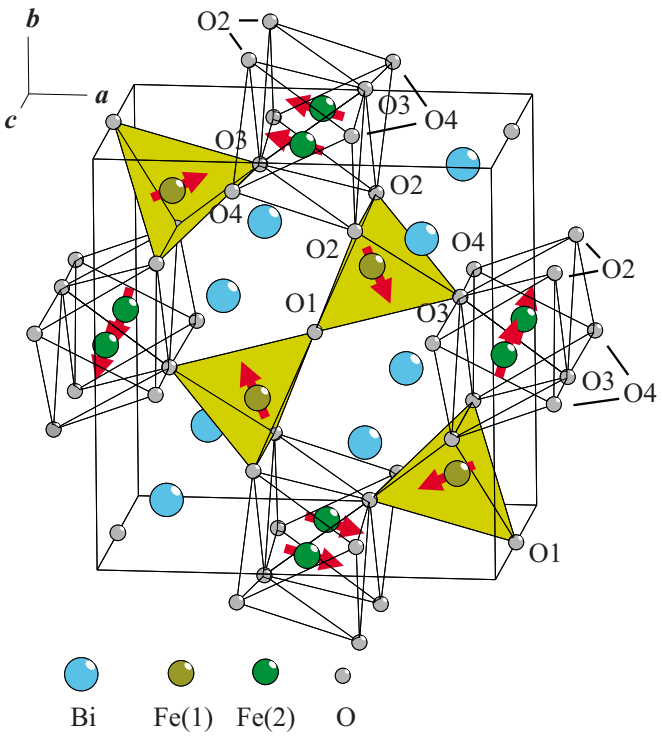

FIG. 1. (Color online) The unit cell of $Bi_2Fe_4O_9$. The direction of magnetic moment in the antiferromagnetic state are also shown.

The bismuth-based complex oxides with mullite-type structure, $Bi_2Fe_4O_9$, $Bi_2Al_4O_9$, $Bi_2Ga_4O_9$, and $Bi_2Mn_4O_{10}$ attract considerable interest as functional materials with potential applications in solid oxide fuel cells, sensors, scintillators, etc.[4,5] Additional stimulus for more detailed study of the compounds containing transitional metal is the reported multiferroic behavior of $Bi_2Mn_4O_{10}$ (Ref. 6) and $Bi_2Fe_4O_9$.[7]

In this work we present results of a detail Raman-scattering study of $Bi_2Fe_4O_9$ single crystals in a broad temperature range (10–300 K). The symmetry of all first-order Raman phonon lines was identified and they were assigned to definite atomic motions by comparison to calculated frequencies and eigenvectors of the modes of same symmetry. Strongly resonant two-phonon scattering was observed in the Raman spectra measured from the *ab*—(001) surface. In addition to the phonon lines, broad temperature-dependent bands, exhibiting the characteristics of magnon scattering were present in the low-temperature spectra. The nature and behavior of magnon bands is discussed on the basis of magnetic structure of $Bi_2Fe_4O_9$.

II. SAMPLES AND EXPERIMENT

Single crystals of $Bi_2Fe_4O_9$ crystals were grown by the high temperature solution growth method. The starting materials, were Bi_2O_3, Fe_2O_3, and Bi_2O_3 flux (minimum purity

 ©2010 The American Physical Society

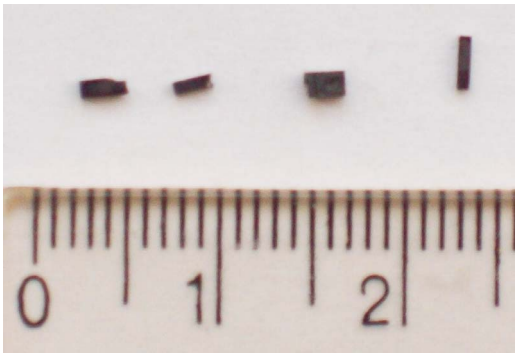

FIG. 2. (Color online) As-grown single crystals of $Bi_2Fe_4O_9$. Most of the natural edges are along ⟨110⟩ or ⟨001⟩ crystallographic directions.

of 99.999%), at ratio 7:1 of flux to crystallizing compound, were placed in a platinum crucible (R=60 mm, L =75 mm) covered with platinum lid and melted at 1150 °C. The crystal growth was accomplished by cooling the high-temperature solution to 870 °C at a cooling rate of 0.5 °C/h. At 870 °C the flux was removed from the crucible by decanting. The $Bi_2Fe_4O_9$ crystallized on the wall of the crucible with maximum crystal dimensions $2\times3\times5$ mm^3 (see Fig. 2). The x-ray powder-diffraction patterns were indexed within the orthorhombic *Pbam* (No. 55) space group with unit-cell parameters: a=7.967 Å, b=8.443 Å, and c =5.996 Å.

The magnetic response to dc-magnetic field illustrated in Fig. 3 was measured by Quantum Design's superconducting quantum interference device. Several crystals were probed and all showed antiferromagnetic transition at T_N =237±1 K, a temperature somewhat below the T_N =265±3 K reported for powder samples[3,8] but in a good agreement with the data available for single crystals.[9] The magnetic susceptibility was found to obey the Curie-Weiss law, (not shown here), with $\theta\approx-1670$ K.[2]

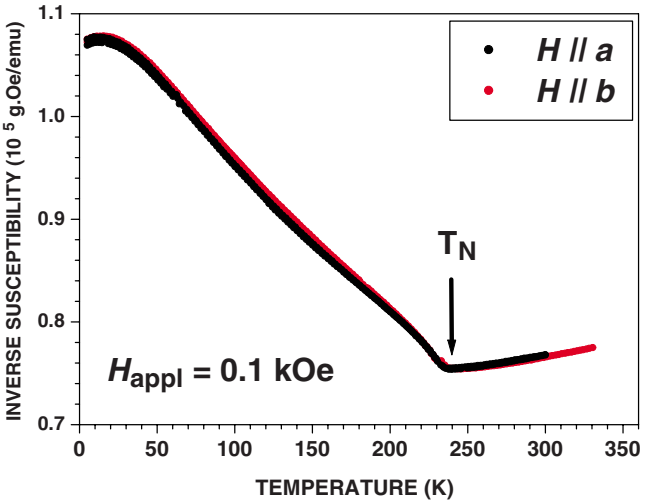

FIG. 3. (Color online) Inverse magnetic susceptibility of $Bi_2Fe_4O_9$ as measured with weak dc field along the a and b axes.

The Raman spectra were measured from natural (001), (100), (010), and (110) surfaces of $Bi_2Fe_4O_9$ single crystals using a triple Raman spectrometer T64000 (Horiba Jobin Yvon) equipped with microscope, optical cryostat, charge coupled device detector, and Ar^+ and He-Ne laser sources. After the crystallographic directions $x\equiv[100]$, $y\equiv[010]$, and $z\equiv[001]$ were identified, the spectra could be measured with exact $z(xx)\bar{z}$, $z(yy)\bar{z}$, $z(xy)\bar{z}$, $y(xx)\bar{y}$, $y(zz)\bar{y}$, $y(xz)\bar{y}$, and $x(yz)\bar{x}$ scattering configurations. Based on the polarization-selection rules for the phonon modes of $A_g(xx,yy,zz)$, $B_{1g}(xy)$, $B_{2g}(xz)$, and $B_{3g}(yz)$ symmetry, the classification by symmetry of all observed Raman lines could easily be done.

III. PHONON CLASSIFICATION AND CALCULATION PROCEDURES

A. Γ-point Raman phonons

In Table I are shown the atomic-site symmetries and the

TABLE I. Wyckoff notations and irreducible representations for the nonequivalent atomic sites in the *Pbam* structure of $Bi_2Fe_4O_9$ (Refs. 10 and 11).

Atom	Wyckoff notation	Irreducible representantions
Bi	4*g*	$2A_g+A_u+2B_{1g}+B_{1u}+B_{2g}+2B_{2u}+B_{3g}+2B_{3u}$
Fe1	4*h*	$2A_g+A_u+2B_{1g}+B_{1u}+B_{2g}+2B_{2u}+B_{3g}+2B_{3u}$
Fe2	4*f*	$A_g+A_u+B_{1g}+B_{1u}+2B_{2g}+2B_{2u}+2B_{3g}+2B_{3u}$
O1	2*b*	$A_u+B_{1u}+2B_{2u}+2B_{3u}$
O2	8*i*	$3A_g+3A_u+3B_{1g}+3B_{1u}+3B_{2g}+3B_{2u}+3B_{3g}+3B_{3u}$
O3	4*h*	$2A_g+A_u+2B_{1g}+B_{1u}+B_{2g}+2B_{2u}+B_{3g}+2B_{3u}$
O4	4*g*	$2A_g+A_u+2B_{1g}+B_{1u}+B_{2g}+2B_{2u}+B_{3g}+2B_{3u}$

Modes classification

$\Gamma_{\text{Raman}}=12A_g+12B_{1g}+9B_{2g}+9B_{3g}$	$\Gamma_{\text{ir}}=8B_{1u}+14B_{2u}+14B_{3u}$
$A_g\rightarrow\alpha_{xx},\alpha_{yy},\alpha_{zz}$	$\Gamma_{\text{silent}}=9A_u$
$B_{1g}\rightarrow\alpha_{xy},\alpha_{yx}$	$\Gamma_{\text{acoustic}}=B_{1u}+B_{2u}+B_{3u}$
$B_{2g}\rightarrow\alpha_{xz},\alpha_{zx}$	
$B_{3g}\rightarrow\alpha_{yz},\alpha_{zy}$	

TABLE II. Short-range potentials and shell-model parameters for $Bi_2Fe_4O_9$. The cut-off radius is set to 12 Å.

Ion	$Y(\|e\|)$	$Q(\|e\|)$	k (eV Å^{-2})	Ion pair	a (eV)	r_0 (Å)	c (eV Å^6)
Bi	3.35	−0.5000	451.0	Bi-O	4320	0.277	0
Fe	3.95	−0.5375	30.00	Fe-O	4390	0.246	0
O	0.80	−2.9500	74.92	O-O	22 764	0.149	27.9

participation of different types of atoms in zone-center (Γ-point) phonon modes. Of the in total 90 zone-center modes, $42(12A_g+12B_{1g}+9B_{2g}+9B_{3g})$ are Raman active.[10,11] The Raman polarization-selection rules, which allow determination of the symmetry of a given Raman lines are also given.

B. Lattice dynamical calculations

Lattice dynamical calculations (LDC) for $Bi_2Fe_4O_9$ were performed within shell model using the general utility lattice program (GULP).[12] In the shell model the ion is considered as a point core with charge Y surrounded by a massless shell with charge Q. The free ion polarizability is accounted for by the force constant k. The interionic interactions are described by long-range Coulomb potentials and short-range potentials $V(r)$, the latter chosen in the Born-Mayer-Buckingham form

$$V(r) = a\exp(-r/r_0) - cr^{-6},$$

where r is the interatomic distance. The cation-anion short-range interactions usually contain no attractive part, i.e., $c=0$ in the expression for $V(r)$. The Coulomb energy calculations are based on a real-space summation involving a spherical cut-off boundary (characterized by a cut-off radius) that makes the sum of all charges within the spherical cut-off region equal to zero.[13] As starting point we used the crystallographic data reported in Ref. 2 and well-documented potentials and interionic interactions for Fe and O ions.[14] Bi and Bi-O parameters are very close to those previously used for $BiFeO_3$ compounds.[15] Best fit to the experimental Raman

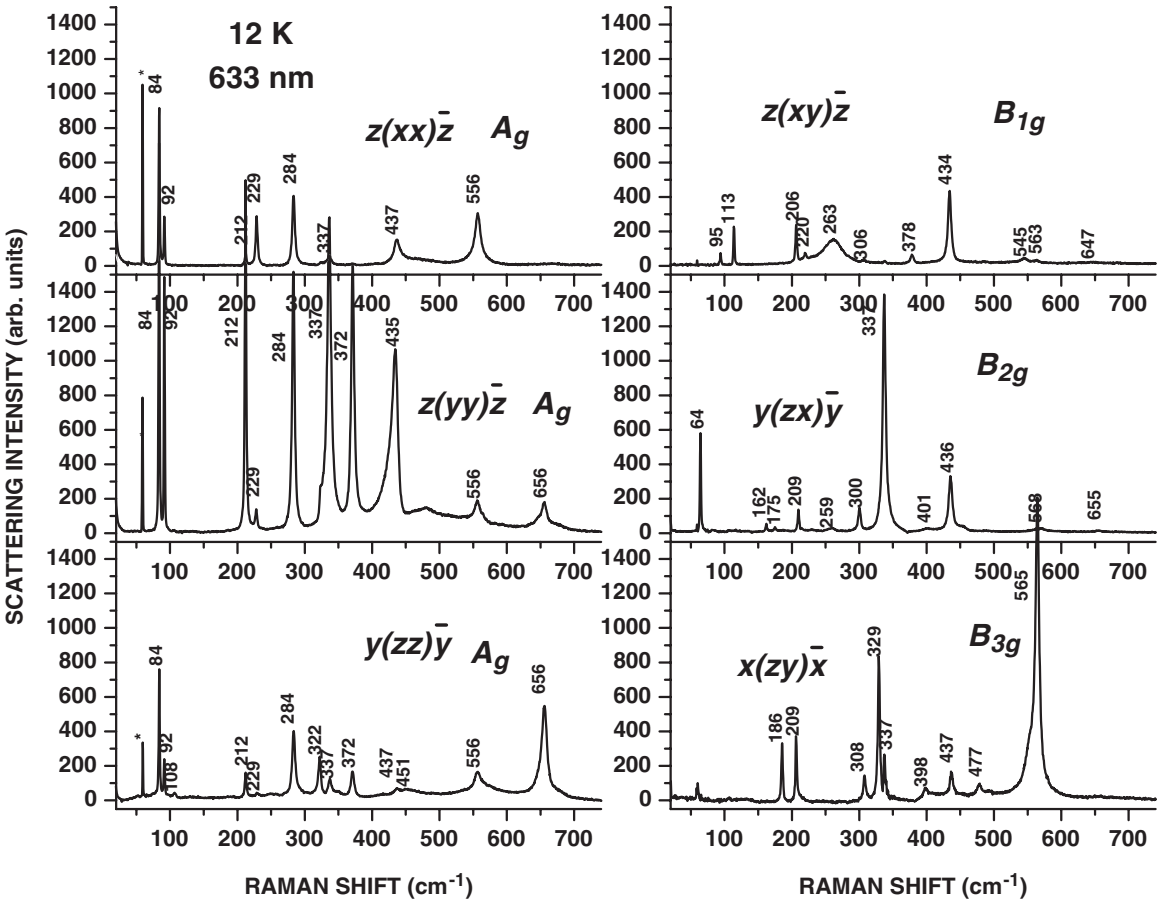

FIG. 4. Polarized Raman spectra of $Bi_2Fe_4O_9$ as obtained at 12 K with 633 nm excitation.

TABLE III. Calculated and experimentally determined frequencies (in cm^{-1}) of the Raman-active modes in $Bi_2Fe_4O_9$.

Mode	Theoretical LDC	Experiment 12 K/300 K	Atomic motions
$A_g(1)$	88	84/81	Bi (xy plane)
$A_g(2)$	117	92/87	Bi (xy plane)
$A_g(3)$	252	212/207	Fe1 (xy plane)
$A_g(4)$	297	229/222	O2(xy)+O3(y)
$A_g(5)$	389	322/317	Fe2(z)
$A_g(6)$	395	337/331	O3(xy)
$A_g(7)$	430	372/365	O4(z)+O3(xy)
$A_g(8)$	497	437/430	O3(xy)+Fe2(xy)
$A_g(9)$	517	556/552	
$A_g(10)$	595	656/647	O4(xy)
$A_g(11)$	687	735/726	O3(xy)
$A_g(12)$	813	825/810	O2(yz)
$B_{1g}(1)$	106	95/92	Bi(x)
$B_{1g}(2)$	121	113/110	Bi(y)
$B_{1g}(3)$	237	206/202	Fe1(xy)+O2(xy)
$B_{1g}(4)$	326	306/283	O3(y)
$B_{1g}(5)$	384	337/330	O3(xy)n
$B_{1g}(6)$	440	378/367	O4(x)+Fe2(z)n
$B_{1g}(7)$	465	434/430	O4(xy)
$B_{1g}(8)$	545	544/537,555	O4(xy)+O3(xy)
$B_{1g}(9)$	606	637/641	O4(xy)+g
$B_{1g}(10)$	628	685/671	O4(xy)+O2(xy)s
$B_{1g}(11)$	714	754/735	O3(xy)
$B_{1g}(12)$	834	826/811	O2(yz)
$B_{2g}(1)$	100	64/61	Bi(x)
$B_{2g}(2)$	107	162/159	O4(z)
$B_{2g}(3)$	233	209/205	O2(xz)+O3(z)
$B_{2g}(4)$	283	259	O4(z)+O3(z)s
$B_{2g}(5)$	305	300	O3(z)+Fe2(xy)
$B_{2g}(6)$	381	337/328	O2(y)
$B_{2g}(7)$	492	436/431	O2(xy)+O3(z)
$B_{2g}(8)$	562		O3(z)+O4(z)
$B_{2g}(9)$	756		O3(yz)
$B_{3g}(1)$	87		O4(z)+Bi(z)s
$B_{3g}(2)$	122	186/182	O4(z)+Fe2(xy)
$B_{3g}(3)$	227	209/205	O4(z)+O3(z)+O2
$B_{3g}(4)$	274	308/301	Fe2(y)
$B_{3g}(5)$	288	398	O3(z)+O2(xy)
$B_{3g}(6)$	414	437/431	O2
$B_{3g}(7)$	480	477/472	O2
$B_{3g}(8)$	570	565/556	O3(z)+O4(z)
$B_{3g}(9)$	758		O2(yz)

frequencies of $Bi_2Fe_4O_9$ was obtained with the parameters listed in Table II. The calculated frequencies and the main atomic motions involved the Raman modes are given in Table III.

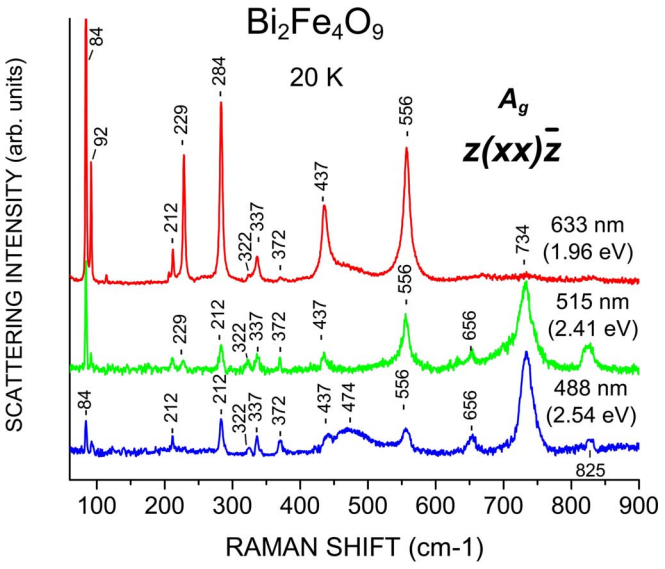

FIG. 5. (Color online) $z(xx)\bar{z}$ spectra of $Bi_2Fe_4O_9$ measured at 20 K with 488 nm (2.54 eV), 515 nm (2.41 eV), and 633 nm (1.96 eV) excitation.

IV. EXPERIMENTAL RESULTS AND DISCUSSION

A. First-order Raman spectra

Figure 4 shows the polarized Raman spectra of $Bi_2Fe_4O_9$ as obtained at 12 K with 633 nm (1.96 eV) excitation. The phonon frequencies are compared to LDC predicted ones in Table III. The agreement between experimental and predicted values is relatively good for the low-frequency modes, dominated by Bi vibrations, and high-frequency modes, involving mainly oxygen-stretching motions but more ambiguous for the modes between 200 and 400 cm^{-1}, where the eigenvectors are more complex. The absolute and relative intensities of Raman lines depend significantly on the excitation photon energy. As illustrated in Fig. 5, at comparable incident laser power density of 633 nm (1.96 eV), 515 nm (2.41 eV), and 488 nm (2.54 eV) excitation, most of the lines are much stronger in the 633 nm spectra. On the other hand side, the spectra with 515 and 488 nm excitation are very similar with most pronounced band at 734 cm^{-1}. Such strongly resonant behavior is most likely linked to the electronic d-d transition between the levels of Fe^{3+} splitted by $\approx$2.6 eV in the octahedral and/or tetrahedral crystal field.[16–19]

B. Second-order spectra: Franck-Condon effect

The most dramatic effect of changing the excitation photon energy from 1.96 eV (633 nm) to 2.41 eV (515 nm) or 2.54 eV (488 nm) is the appearance of strong second-order scattering with main characteristics as follows: (i) the second-order spectra are observed for light polarizations parallel to the ab plane (xx, yy, and xy) but not perpendicular to it (zz, zx, and zy); (ii) the second-order spectral profiles between 1000 and 1700 cm^{-1} are almost exact replicas of corresponding first-order spectra between 500 and 850 cm^{-1}; and (iii) the intensities of second-order lines are comparable to those of their first-order counterparts.

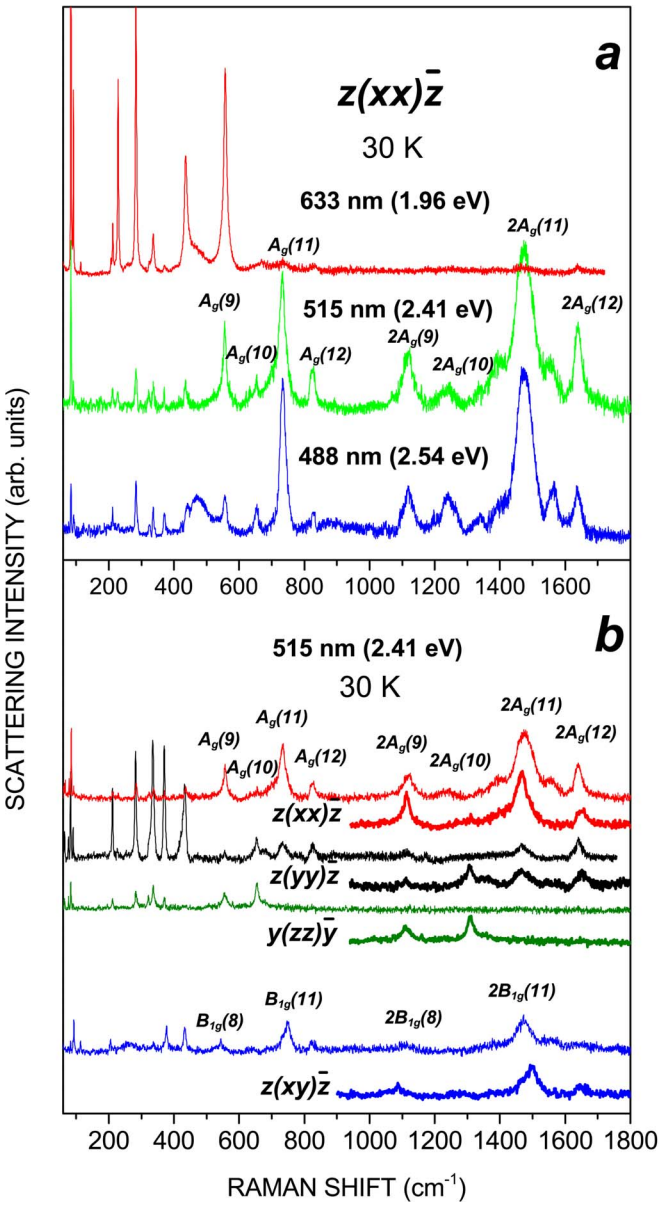

FIG. 6. (Color online) First and second-order Raman spectra of $Bi_2Fe_4O_9$: (a) the dependence of the excitation photon energy and (b) the dependence on the scattering configuration.

The specifics of the second-order scattering is illustrated in Fig. 6. The shorter spectral segments between 900 and 1800 cm^{-1} in Fig. 6(b) represent the spectra between 450 and 900 cm^{-1} if the frequency is multiplied by factor of 2. The temperature has little effect on the characteristics of second-order scattering: the spectral lineshape remains practically the same up to room temperature and the second-order peak intensities undergo the same decrease as the first-order counterparts. This is illustrated in Fig. 7 for the $z(xx)\bar{z}$ spectra with 488 nm excitation.

The supposed electronic structure of $Bi_2Fe_4O_9$ and the characteristics of the second-order Raman spectra provide strong indications that the multiple scattering can find explanation in terms of the Franck-Condon effect applied to the excitation and decay of *d-d* electronic excitations of Fe^{3+} ion. Indeed, unlike the isostructural $Bi_2Ga_4O_9$, which is

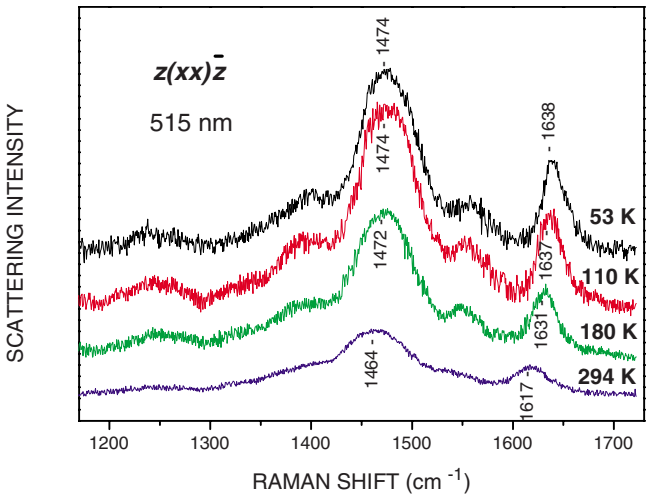

FIG. 7. (Color online) Second-order Raman spectra of $Bi_2Fe_4O_9$ at various temperatures.

transparent in the visible range[20] and has similar Raman spectra, $Bi_2Fe_4O_9$ is an opaque material, the absorption being caused by transitions between the $3d^5$ levels of Fe^{3+} split by tetrahedral or octahedral crystal field.[21] Although no experimental data or calculations on the *d-d* transitions in $Bi_2Fe_4O_9$ are available, it is reasonable to assume that the *d-d* transition energies are close to those of other materials containing $Fe^{3+}O_6$ octahedra and $Fe^{3+}O_4$ tetrahedra, such as $Y_3Fe_5O_{12}$ or $Y_3Ga_{5-x}Fe_xO_{12}$.[16,17,19] In the photon-energy range of interest (1.9–2.6 eV) are the transitions from the ground ${}^6S(A_{1g}/A_1)$ state of $Fe^{3+}(d^5)$ to the first excited ${}^4G(T_{1g}/T_1)$ and ${}^4G(T_{2g}/T_2)$ states splitoff by the orthohedral/tetrahedral crystal field. In octahedral field the transitions between ${}^6S$ and any ${}^4G$ manifold levels are parity forbidden, which results in very weak absorption. The lack of inversion at tetragonal sites, however, allows mixing with higher-energy odd-parity states thus relaxing the parity constrains and rising the absorption coefficient. These general considerations are confirmed experimentally and theoretically for $Y_3Fe_5O_{12}$, where the weak absorption between 1.2 and 2.2 eV and abrupt absorption rise above 2.4 eV have been assigned to ${}^6S \rightarrow {}^4G$ crystal-field transitions, respectively, in $Fe^{3+}O_6$ octahedra and $Fe^{3+}O_4$ tetrahedra.[16,17,19]

In the time scale of phonon vibrations an electronic transition is essentially instantaneous, which means that immediately after the transition the atomic positions are the same as in the initial state. The final state, however, requires different equilibrium position, which is achieved by the Franck-Condon process of phonon emission as illustrated in Fig. 8.

Applied to the Raman scattering the Franck-Condon process manifests itself in appearance of multiphonon bands, which replicate the first-order spectrum of participating phonons. The theoretical aspects of this type of scattering have been discussed in detail by Allen and Perebeinos[22,23] on the example of $LaMnO_3$. In particular, it has been shown that the second-order scattering may be stronger than the first-order one while the higher-order phonon bands are much weaker. This is exactly what we observe in the Raman spectra of $Bi_2Fe_4O_9$.

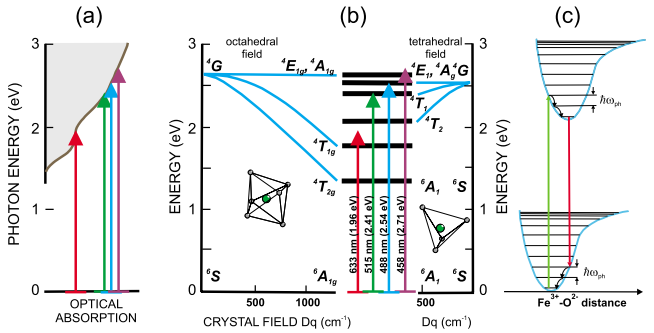

FIG. 8. (Color online) Franck-Condon effect energy diagram.

C. Magnon scattering

The magnetic ordering below $T_N \approx 240$ K has little effect on the phonon-line parameters but gives rise to new broad Raman bands, which are mostly consistent with magnon scattering. These are the band at 260 cm^{-1} pronounced in the $z(xy)\bar{z}$ spectra and the band at 472 cm^{-1}, most clearly seen in the xx spectra with 488 nm excitation. The temperature dependence of the 260 cm^{-1} band and its parameters (position, width, and integrated intensity) are presented in Figs. 9(a) and 9(b). The $z(xx)\bar{z}$ spectra, where at low temperatures the second magnon band is observed with 488 nm (2.54 eV) excitation, are shown in Fig. 9(c).

Based on their relatively high frequency (>250 cm^{-1}), it is unlikely that the magnetic-order-induced bands correspond to one-magnon excitations, i.e., single spin-flip processes with wave vectors at the center of the Brillouin zone. For comparison the zone-center magnons in rare-earth orthoferrites $RFeO_3$ (R=Dy,Ho,Er,Sm) have frequencies below 25 cm^{-1}.[24] It would be more realistic to analyze the magnetic excitations in $Bi_2Fe_4O_9$ under the assumption that they involve two-magnon processes, like in the well-known cases of ferrites[25] or cuprates.[26,27]

The magnetic structure of $Bi_2Fe_4O_9$ is rather peculiar due to the geometrical frustration imposed on the antiferromagnetic (AFM) alignment of spins at Fe1 (tetrahedral positions) and Fe2 (octahedral positions) sites.[2] A definite indication for such a frustration is seen in the high-frustration index[28] $f = |\theta|/T_N \approx 7$ of $Bi_2Fe_4O_9$. The directions of the magnetic moments of $Bi_2Fe_4O_9$ in the ab plane, as obtained from the refinement of single-crystal diffraction data,[2] are shown in Fig. 10, where the solid and empty arrows denote the magnetic moments (or spins) of Fe1 and Fe2 ions, respectively. The spins of Fe1 ions form two interconnected distorted hexagonal spin webs with spin directions in each web orthogonal to those in the other web. The intersections of the two spin webs are at the Fe2 sites. In the ordered AFM state, the two sets of magnetic ions are apparently magnetically nonequivalent. For instance, in the ab plane only the ions at Fe1 sites interact with each other through the nearest-neighbor (NN) super-exchange interactions denoted in Fig. 10 as J_{11} whereas Fe2-Fe2 magnetic interactions are of the next-nearest-neighbor type via F1 atoms, i.e., involving Fe1-Fe2 (NN), J_{12} and J'_{12} interactions. The Fe2-Fe2 (NN), J_{22} and J'_{22}, interaction are along the c axis of the structure (see also Fig. 1). This particular interconnection between the spins at the Fe1 and Fe2 sites implies relatively strong intersite magnetic interactions consistently with the observed single magnetic transition temperature. On the other hand, the spin web connecting all Fe atoms through the (NN) interaction paths forms a distorted pentagonal lattice, yet another manifestation of magnetic frustration.[2]

The magnetic structure shown in Fig. 10 can be decomposed into eight spin sublattices paired antiferromagnetically to form four AFM lattices, two for each iron site. For a given Fe site, the magnetic alignment in each one of the AFM lattices is orthogonal to the other due to magnetic frustration. To the best of our knowledge, there are no model calculations of Raman-active magnetic excitations in frustrated AFM structures that could resemble that of $Bi_2Fe_4O_9$. Therefore at this stage we can analyze only qualitatively the magnetic excitations in this material.

As we already mentioned above the Raman magnon bands at 260 and 472 cm^{-1} are consistent with two-magnon Raman scattering. In this scattering process the incident light creates two magnons simultaneously, one on each of the two

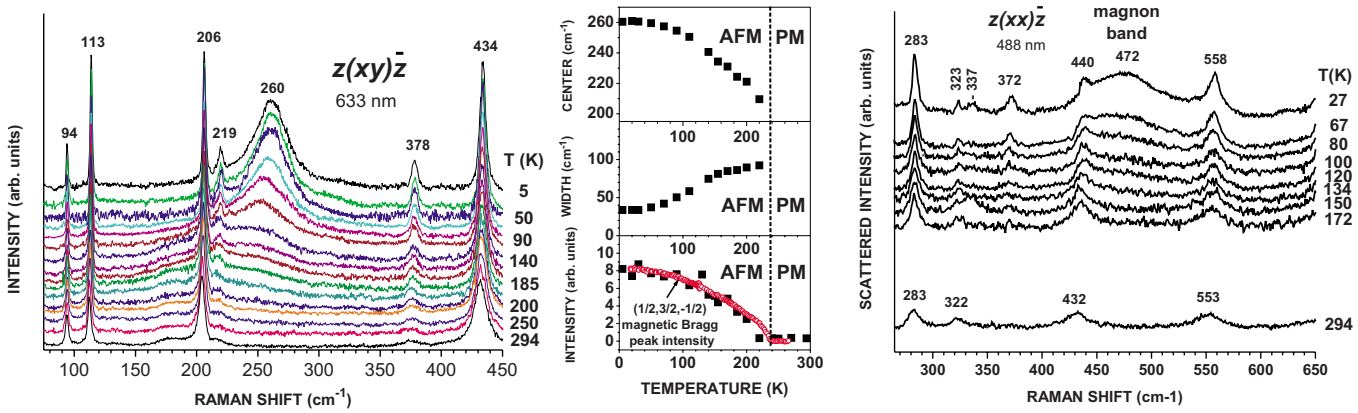

FIG. 9. (Color online) (a) Temperature dependence of the 260 cm^{-1} magnon band in the $z(xy)\bar{z}$ spectra as measured with 633 nm (1.96 eV) excitation. (b) Variations with T of the 260 cm^{-1} magnon band maximum, width, and integrated intensity. In the lowest panel is also shown the temperature variation in the $(\frac{1}{2},\frac{3}{2},\frac{-1}{2})$ magnetic Bragg peak in zero field from neutron diffraction. (c) Temperature dependence of the 472 cm^{-1} magnon band in the $z(xx)\bar{z}$ spectra measured with 488 nm (2.54 eV) excitation.

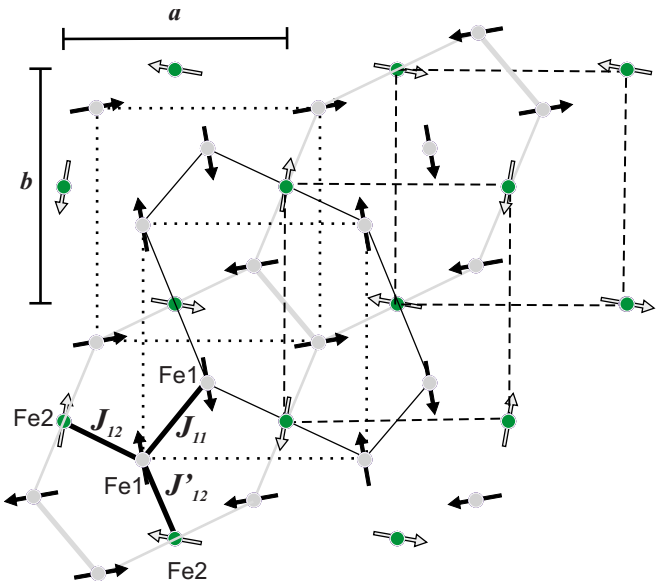

FIG. 10. (Color online) Magnetic structure of $Bi_2Fe_4O_9$ as it is suggested in Ref. 2. The solid and empty arrows denote the magnetic moments of Fe ions at the Fe1 and Fe2 sites, respectively. The dotted frames mark the unit cells of two AFM lattices of Fe1 ions. The dashed frames border the unit cells of the Fe2 AFM lattices.

sublattices of a AFM lattice. In order to be a Raman-active excitation, the two-magnon mode should have zero total wave vector (momentum), i.e., the two magnons have opposite wavevectors $\mathbf{k},-\mathbf{k}$. Among the pairs of magnons with zero total momentum those around the van Hove singularities (vHS) in the two-magnon density of states contribute strongly in the Raman process. Typically, the magnon states at the magnetic Brillouin-zone (BZ) boundary create vHS in the two-magnon density of states. In the real space, the Raman scattering from a pair of magnons with wave vectors on the BZ boundary corresponds to a double spin flip on adjacent magnetic ions. In the case of a collinear Heisenberg antifferomagnet with unfrustrated (NN) exchange the two-magnon peak is expected at $\omega_{2M}=2zSJ-J$, where z is the coordination number, S is the spin number, and J is the AFM exchange energy. The reduction in the two-magnon energy by J is due to the exchange link between the (NN) sites, i.e., involving the final-state magnon-magnon interactions. The Raman scattering from frustrated AFM structures have been studied theoretically very little. Recent theoretical work on Raman scattering from a AFM on triangular lattice shows that the main Raman peak is in approximately the center of the two-magnon density of states whereas the second peak close to ω_{2M} is much weaker.[29–31] The authors of Ref. 30 also demonstrate that accounting for the noncollinearity in the spin ground state requires nontrivial corrections (renormalization) of the spin-wave spectrum to the first order of $1/S$.

Generally, a theoretical study of the Raman-active magnetic excitations in $Bi_2Fe_4O_9$ could be even more complicated than that in Refs. 29 and 30. The mean-field calculations with five (NN) superexchange interactions with the energies J_{11}, J_{12}, J'_{12}, J_{22}, and J'_{22} reproduces well the magnetic structure shown in Figs. 1 and 10, provided $J_{12}\approx 2J'_{12}$ and $J_{12}\geq J_{11}$.[2] For the magnetic structure given in Fig. 10 one may expect three types of double spin-flip excitations on neighboring Fe ions—one Fe1-Fe1 (NN) and two for Fe1-Fe2 (NN). The corresponding two-magnon energies are $\omega_{2M}(\mathrm{Fe1-Fe1})=2S(J_{11}+3J_{12})-J_{11}$, $\omega_{2M}(\mathrm{Fe1-Fe2})=2S(J_{11}+3J_{12})-J_{12}$, and $\omega_{2M}(\mathrm{Fe1-Fe2'})=2S(J_{11}+3J_{12})-(1/2)J_{12}$. Given $S=5/2$, the energy of these two-magnon excitaions will differ little. One possibility is to assign the broad Raman band at 470 cm^{-1} to two-magnon scattering with energy ω_{2M} involving all the pair excitations of Fe1-Fe1, Fe1-Fe2, and Fe1-Fe2′. The 470 cm^{-1} band intensity is expected to be very weak if one follows the analogy with the two-magnon Raman scattering in triangular lattices.[29,30] Notably, this band has no detectable intensity when excited with the 633 nm laser line. The appearance of the band under 488 nm laser excitation could be related to the enhanced absorbtion of Fe^{3+} in both Fe1 and Fe2 sites (see, e.g., Fig. 8). Then, the two-magnon band at 260 cm^{-1} could be related to scattering processes similar to those that create the "lower-frequency" Raman peak at about $\frac{1}{2\omega_{2M}}$ in the case of triangular lattices.[29,30] This assignment of the two-magnon Raman bands in $Bi_2Fe_4O_9$ is very tentative. More extensive studies are needed, both theoretical and experimental, in order one to find out the mechanisms behind the magnetic excitations in this material.

V. CONCLUSIONS

The lattice dynamics calculations and polarized Raman-scattering measurements presented in this work consistently describe in detail the origin of the Raman modes in $Bi_2Fe_4O_9$. The two Raman bands at 260 and 470 cm^{-1} are shown to have magnetic origin and being related to two-magnon scattering.

ACKNOWLEDGMENTS

This work was supported in part under Grant No. TK-X-1712/2007 by the Bulgarian Science Fund and by the State of Texas through the Texas Center for Superconductivity at the University of Houston.

[1] N. Niizeki and M. Wachi, Z. Kristallogr. **127**, 173 (1968).
[2] E. Ressouche, V. Simonet, B. Canals, M. Gospodinov, and V. Skumryev, Phys. Rev. Lett. **103**, 267204 (2009).
[3] N. Shamir, E. Gurewitz, and H. Shaked, Acta Crystallogr., Sect. A: Cryst. Phys., Diffr., Theor. Gen. Crystallogr. **34**, 662 (1978).
[4] V. V. Volkov and A. V. Egorysheva, Opt. Mater. **5**, 273 (1996).
[5] S. Zha, J. Chang, X. Liu, and G. Meng, Solid State Ionics **156**, 197 (2003).
[6] D. K. Shukla, S. Mollah, Ravi Kumar, P. Thakur, K. H. Chae, W. K. Choi, and A. Banerjee, J. Appl. Phys. **104**, 033707 (2008).

[7] A. K. Singh, S. D. Kaushik, Brijesh Kumar, P. K. Mishra, A. Venimadhav, V. Siruguri, and S. Patnaik, Appl. Phys. Lett. **92**, 132910 (2008).
[8] V. A. Bokov, S. I. Yushchuk, G. V. Popov, N. N. Parfenova, and A. G. Tutov, Sov. Phys. Solid State **13**, 1333 (1971).
[9] D. M. Giaquinta, G. C. Papaefthymiou, W. M. Davis, and H.-C. Zur Loye, J. Solid State Chem. **99**, 120 (1992).
[10] M. I. Aroyo, J. M. Perez-Mato, C. Capillas, E. Kroumova, S. Ivantchev, G. Madariaga, A. Kirov and H. Wondratschek, Z. Kristallog. **221**, 15 (2006).
[11] M. I. Aroyo, A. Kirov, C. Capillas, J. M. Perez-Mato, and H. Wondratschek, Acta Crystallogr., Sect. A: Cryst. Phys., Diffr., Theor. Gen. Crystallogr. **62**, 115 (2006).
[12] G. D. Gale, J. Chem. Soc., Faraday Trans. **93**, 629 (1997).
[13] D. Wolf, P. Keblinski, S. R. Philpot, and J. Eggebrecht, J. Chem. Phys. **110**, 8254 (1999).
[14] T. S. Bush, J. D. Gale, C. R. A. Catlow, and P. D. Battel, J. Mater. Chem. **4**, 831 (1994).
[15] M. O. Ramirez, A. Kumar, S. A. Denev, Y. H. Chu, J. Seidel, L. W. Martin, S.-Y. Yang, R. C. Rai, X. S. Xue, J. F. Ihlefeld, N. J. Podraza, E. Saiz, S. Lee, J. Klug, S. W. Cheong, J. M. Bedzyk, O. Auciello, D. G. Schlom, J. Orenstein, R. Ramesh, J. L. Musfeldt, A. P. Litvinchuk, and V. Gopalan, Appl. Phys. Lett. **94**, 161905 (2009).
[16] G. B. Scott, D. E. Lacklison, and J. L. Page, Phys. Rev. B **10**, 971 (1974).
[17] T. K. Vien, J. L. Dorman, and H. Legall, Phys. Status Solidi B **71**, 731 (1975).
[18] W. F. J. Fontijn, P. J. van der Zaag, and R. Metselaar, J. Appl. Phys. **83**, 6765 (1998).
[19] Zhou Kang-Wei, Xie Jun-Kai, Ning Yo-Ming, Zhao Sang-Bo, and Wu Ping-Feng, Phys. Rev. B **44**, 7499 (1991).
[20] A. Beran, E. Libowitzky, M. Burianek, M. Mühlberg, C. Pecharromán, and H. Schneider, Cryst. Res. Technol. **43**, 1230 (2008).
[21] L. E. Orgel, J. Chem. Phys. **23**, 1004 (1955).
[22] P. B. Allen and V. Perebeinos, Phys. Rev. Lett. **83**, 4828 (1999).
[23] V. Perebeinos and P. B. Allen, Phys. Rev. B **64**, 085118 (2001).
[24] R. M. White, R. J. Nemanich, and C. Herring, Phys. Rev. B **25**, 1822 (1982).
[25] M. J. Massey, U. Baier, R. Merlin, and W. H. Weber, Phys. Rev. B **41**, 7822 (1990).
[26] A. P. Litvinchuk, L. Börjesson, C. Thomsen, and C. W. Chu, Phys. Status Solidi B **215**, 507 (1999).
[27] J. Holmlund, C. S. Knee, J. Andreasson, M. Granath, A. P. Litvinchuk, and L. Börjesson, Phys. Rev. B **79**, 085109 (2009).
[28] A. P. Ramirez, Annu. Rev. Mater. Sci. **24**, 453 (1994).
[29] F. Vernay, T. P. Devereaux, and M. J. P. Gingras, J. Phys.: Condens. Matter **19**, 145243 (2007).
[30] N. Perkins and W. Brenig, Phys. Rev. B **77**, 174412 (2008).
[31] J. B. Parkinson, J. Phys. C **2**, 2012 (1969).